LEVERAGING NOMA AND ARTIFICIAL NOISE IN SECURE STAR-RIS-ASSISTED UAV-MEC NETWORKS

KHAI THÁC KỸ THUẬT NOMA VÀ PHÁT NHIỄU NHÂN TẠO TRONG MẠNG TRUYỀN THÔNG BẢO MẬT MEC STAR-RIS UAV

Thanh-Nam Nguyen, Van-Truong Truong*

Duy Tan University, Da Nang, Vietnam

*Corresponding author: truongvantruong@dtu.edu.vn

(Received: February 08, 2025; Revised: April 15, 2025; Accepted: April 25, 2025)

DOI: 10.31130/ud-jst.2025.047E

Abstract - This paper investigates a mobile edge computing (MEC) network empowered by non-orthogonal multiple access (NOMA) to enhance security and reduce computational load. The system comprises an unmanned aerial vehicle (UAV), a simultaneously transmitting and reflecting reconfigurable intelligent surface (STAR-RIS), two access points (APs), and a passive eavesdropper. The STAR-RIS employs an energy splitting (ES) protocol, enabling its elements to simultaneously reflect and transmit signals. To enhance physical-layer security, the UAV generates artificial noise (AN) to interfere with the eavesdropper, while optimally leveraging the STAR-RIS for directional signal delivery to legitimate APs. The system performance is evaluated based on the secure computation probability, reflecting the likelihood of successful and confidential task offloading. Numerical results demonstrate significant improvements in system security by jointly optimizing UAV altitude and AN power allocation.

Key words - Mobile edge computing; non-orthogonal multiple access; physical layer security; reconfigurable intelligent surfaces; unmanned aerial vehicles

Tóm tắt - Bài báo này nghiên cứu mạng điện toán biên di động hỗ trợ đa truy cập phi trực giao nhằm tăng cường bảo mật và giảm tải tính toán hiệu quả. Hệ thống bao gồm một thiết bị bay không người lái (UAV), một bề mặt thông minh phản xạ - truyền dẫn có thể tái cấu hình (STAR-RIS), hai điểm truy cập (AP) biên và một thiết bị nghe lén thụ động. STAR-RIS sử dụng giao thức phân chia năng lượng (ES) cho phép các phần tử RIS đồng thời thực hiện chức năng phản xạ và truyền dẫn tín hiệu. UAV phát tín hiệu nhiễu nhân tạo (AN) gây nhiễu thiết bị nghe lén, đồng thời tận dụng STAR-RIS với chiến lược phân bổ công suất tối ưu để hướng tín hiệu mong muốn đến các AP. Xác suất tính toán thành công đảm bảo bảo mật được sử dụng làm thông số đánh giá hiệu suất hệ thống. Các kết quả số chứng minh sự cải thiện đáng kể về hiệu suất bảo mật của hệ thống thông qua việc tối ưu hóa độ cao UAV và sử dụng AN.

Từ khóa - Điện toán biên di động; đa truy cập phi trực giao; bảo mật lớp vật lý; bề mặt phản xạ thông minh; phương tiện bay không người lái

1. Introduction

The rapid evolution of wireless communication technologies has facilitated the emergence of novel applications and services, including Industrial IoT, interactive AR/VR, and V2X communication, necessitating ultra-low latency, high reliability, and intelligent edge processing capabilities [1]. Mobile edge computing (MEC) is a promising paradigm for addressing the requirements by strategically positioning computation resources near the network edge [2]. Within the MEC framework, user devices are empowered to offload computationally intensive tasks to nearby edge servers deployed at the base stations or access points (APs). MEC has been demonstrated to effectively integrate with other technologies, enhancing overall efficiency compared to traditional center-cloud computing frameworks [3].

Indeed, the combination of MEC, unmanned aerial vehicles (UAVs), and simultaneously transmitting and reflecting reconfigurable intelligent surfaces (STAR-RISs) brings superior network performance with low latency, high bandwidth, wide coverage, and high flexibility while reducing costs, energy, and enhancing security [4]. UAVs can be deployed as aerial base stations or edge servers to provide on-demand communication and computation services, especially in scenarios where terrestrial infrastructure is limited or unavailable, such as disaster relief, remote areas, and temporary events [2]. Integrating UAVs into MEC networks can further enhance the flexibility and scalability of service provisioning, enabling dynamic resource allocation and optimized network coverage.

However, deploying UAVs in MEC networks poses several challenges, including limited communication range, potential security risks, and interference from other wireless devices. To address these challenges, STAR-RISs can be used to establish communication links between devices that are not in direct line-of-sight, such as a UAV and an AP located on opposite sides of a building, or to enhance the security of wireless communication by reflecting signals towards the intended receiver while transmitting artificial noise (AN) towards potential eavesdroppers [5].

In this paper, we investigate the secrecy performance of a NOMA-assisted MEC network with a UAV and a STAR-RIS, where the UAV offloads its computationally intensive tasks to two APs at the network edge through the STAR-RIS, while a passive eavesdropper attempts to intercept the transmitted information. The main contributions of this paper are summarized as follows:

- We develop a comprehensive system model for a secrecy NOMA-MEC network with a UAV and a STAR-RIS, two computational access points (APs), and one passive eavesdropper, considering large-scale and small-scale fading effects.

- We derive closed-form expressions for the secrecy successful computation probability (SSCP), which characterizes the probability of successfully completing the computation task while ensuring secure communication.

- We provide numerical results to validate our analysis, analyze the impact of key system parameters, and demonstrate the effectiveness of the proposed scheme in enhancing the secrecy performance of the network.

2. System and signal models

2.1. System model

A NOMA MEC network system consisting of a UAV (denoted as ***U***) supported by STAR-RIS (denoted as ***R***), two access points (***APs***) equipped with MEC servers, and a passive eavesdropper (denoted as ***E***) is shown in Figure 1. We assume that ***U*** has limited computing power and needs to offload the task to two access points, i.e., AP_t, AP_r, at the network's edge to support the computing power. Due to the absence of direct links between ***U-APs*** and ***U-E***, attributed to potential obstructions such as buildings or foliage, the STAR-RIS is strategically deployed to establish and enhance these communication channels. Here, all RIS elements operate simultaneously in two modes: transmission mode and reflection mode. Specifically, AP_t resides within the transmission zone of the STAR-RIS, while AP_r and E are situated within its reflection zone. We use the 3D Cartesian coordinate system to describe the coordinates of the nodes in the system model. The coordinates of ***U***, ***R***, AP_t, AP_r, ***E*** are (x_U, y_U, h_U), (x_R, y_R, h_R), $(x_{AP_t}, y_{AP_t}, h_{AP_t})$, $(x_{AP_r}, y_{AP_r}, h_{AP_r})$, and (x_E, y_E, h_E), respectively.

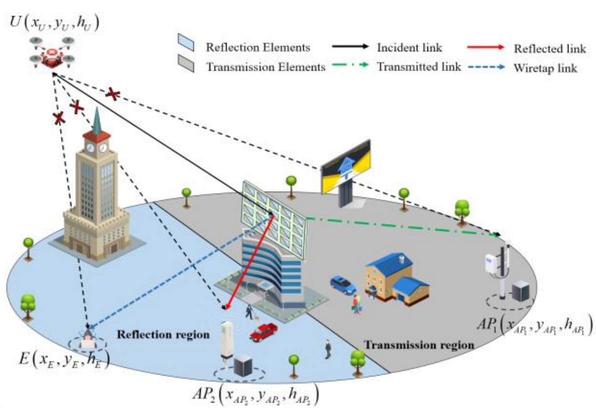

Figure 1. *System model of STAR-RIS-aided NOMA MEC network with UAV and Eavesdropper*

The system model assumes that ***U***, AP_t, AP_r, and ***E*** are all equipped with a single antenna, while the STAR-RIS comprises a fixed array of *N* elements. An energy splitting (ES) protocol is employed at the STAR-RIS, enabling simultaneous reflection and transmission capabilities across all elements [6]. Furthermore, all devices within the network operate in half-duplex mode. Suppose the ***U*** hovers at a fixed height for a very concise period T_{th} to offload the task. Thus, it can be assumed that the change in the UAV's position due to environmental impacts is also minimal [7]. Furthermore, this simple assumption helps us focus on and analyze the fundamental performance trade-offs and benefits introduced by STAR-RIS integration for secure offloading in a UAV-MEC network.

The system under consideration experiences both large-scale and small-scale fading effects. Specifically, large-scale fading, governed by the probabilities of line-of-sight (LoS) and non-line-of-sight (NLoS) propagation, characterizes signal attenuation over extended distances [8]. Accordingly, the mean path loss of LoS and NLoS link for the air-to-ground/ground-to-air model between ***U*** and ***R*** is described as follows [8, 9]:

$$\mathbb{L}_{UR}\left(d_{UR},\theta_{UR}\right)=\left[\mathcal{F}_{NLoS}+\frac{\mathcal{F}_{LoS}-\mathcal{F}_{NLoS}}{1+\zeta e^{-\vartheta\left(\theta_{UR}-\zeta\right)}}\right]d_{UR}^{\alpha}, \quad (1)$$

where $d_{UR}=\sqrt{\left(x_R-x_U\right)^2+\left(y_R-y_U\right)^2+h_U{}^2}$ is the distance between ***U*** and ***R***, α is the path loss exponent, $\theta_{UR}=\frac{180}{\pi}\arcsin\left(\frac{h_U}{d_{UR}}\right)$ denotes elevation angle of ***U*** with respect to ***R***, ζ and ϑ are constant values depending on the environment, $\mathcal{F}_{\mathcal{W}}=\xi_{\mathcal{W}}\left[\left(c/4\pi f_c\right)^{-1}\right]^{\alpha}$, $\xi_{\mathcal{W}}$ is the excessive path loss coefficients in *LoS* and *NLoS* cases, $\mathcal{W}\in\left\{LoS,NLoS\right\}$, *c* represents the speed of light, f_c is the carrier frequency.

Conversely, small-scale fading captures rapid signal fluctuations arising from the interference of reflected, refracted, and scattered waves, modeled as Nakagami-*m* fading [10]. Specifically, $\mathbf{h}_{UR}^{\kappa}\in\mathbb{C}^{N_\kappa\times1}$, $\mathbf{h}_{RAP_\kappa}\in\mathbb{C}^{N_\kappa\times1}$, $\mathbf{h}_{RE}\in\mathbb{C}^{N_r\times1}$ denote the complex channel coefficient from ***U-R***, ***R-APκ***, and ***R-E***, respectively. Here, the symbol κ represents the signal transmission mode with $\kappa\in\left\{t,r\right\}$, i.e. t = tra. and r = ref. To facilitate the mathematical description of STAR-RIS, we define the transmission coefficient matrix and the reflection coefficient matrix as $\Theta^{\kappa}\triangleq\operatorname{diag}\left(\sqrt{\beta_1^{\kappa}}e^{j\phi_1^{\kappa}},\sqrt{\beta_2^{\kappa}}e^{j\phi_2^{\kappa}},\ldots,\sqrt{\beta_{N_\kappa}^{\kappa}}e^{j\phi_{N_\kappa}^{\kappa}}\right)$. $\sqrt{\beta_n^{\kappa}}\in\left[0,1\right]$ is the amplitude-tra. /ref. coefficient and $\phi_n^{\kappa}\in\left[0,2\pi\right)$ is the phase-shift variable of the n^{th} element for transmitting or reflecting responses of STAR-RIS. According to the energy conservation law, the sum of transmitted and reflected signal energy equals the incident signal energy; therefore $\beta_n^t+\beta_n^r=1$ [11]. STAR-RIS is reconfigured with phase shifts to maximize the network performance at the *AP* and maximize the channel power gain, i.e., $\phi_{N_i}^{\kappa}=\arg\left(h_{UR,n}^{\kappa}h_{RY,n}\right)$, $Y\in\left\{AP_t,AP_r,E\right\}$. Accordingly, we can express as follows:

$$\left|\mathbf{h}_{UR}^{\kappa}\Theta^{\kappa}\mathbf{h}_{RY}\right|^2 = \beta^2\left(\sum_{n=1}^{N}\left|h_{UR,n}^{\kappa}\right|\left|h_{RY,n}\right|\right)^2, \quad (2)$$

where $N_\kappa \in \{N_t, N_r\}$ and we assume that $\beta_n^\kappa = \beta, \forall n$ without loss of generality.

To facilitate tracking and computation, the random variable X_Y is denoted as $X_Y = \frac{\left(\sum_{n=1}^{N_\kappa}\left|h_{UR,n}^{\kappa}\right|\left|h_{RY,n}\right|\right)^2}{N(1-\mu_\kappa)}$,

where $\mu_\kappa = \frac{1}{m_{UR}^{\kappa} m_{RY}}\left[\frac{\Gamma\left(m_{UR}^{\kappa}+1/2\right)}{\Gamma\left(m_{UR}^{\kappa}\right)}\right]^2\left[\frac{\Gamma\left(m_{RY}+1/2\right)}{\Gamma\left(m_{RY}\right)}\right]^2$,

$Y \in \{AP_t, AP_r, E\}$. The cumulative distribution function (CDF) and probability density function (PDF) of X_Y are described as follows [12]:

$$F_{X_Y}(x) = e^{-\frac{\lambda_\kappa}{2}}\sum_{l=0}^{\infty}\frac{\lambda_\kappa^l \gamma(l+1/2, x/2)}{l!2^l\Gamma(l+1/2)}, \quad (3)$$

$$f_{X_Y}(x) = e^{-\frac{x+\lambda_\kappa}{2}}\sum_{l=0}^{\infty}\frac{\lambda_\kappa^l x^{l-1/2}}{l!2^{2l+1/2}\Gamma(l+1/2)}, \quad (4)$$

where m_{UR}^{κ}, and m_{RY} are denoted fading parameters, $\lambda_\kappa = \frac{N_\kappa \mu_\kappa}{1-\mu_\kappa}$, $\Gamma(.)$ is the gamma function, and $\gamma(\cdot,\cdot)$ is the lower incomplete gamma function.

2.2. Signal model

According to the principle of NOMA, ***U*** transmits superimposed signal to ***APs*** via STAR-RIS. We assume that ***U*** transmits AN signals and legitimate ***APs*** can decode and remove those while eavesdropping devices will not be able to do this. Thus, the transmit message at ***U*** is expressed as $x_U = \sqrt{\eta_t P_U}x_t + \sqrt{\eta_r P_U}x_r + \sqrt{\eta_j P_U}x_j$, where n_i and n_j are the power allocation coefficients for message x_i and AN signal x_j, respectively, $i \in \{t, r\}$. Note that $\eta_t + \eta_r + \eta_j = 1$. The signal described at AP_κ has the following form:

$$y_{AP_\kappa} = \sqrt{\frac{P_U}{\mathbb{L}_{UR} d_{AP_\kappa}^{\alpha}}}\mathbf{h}_{UR}^{\kappa}\Theta^{\kappa}\mathbf{h}_{RAP_\kappa}x_U + n_\kappa, \quad (5)$$

where P_U is the transmit power of ***U***, d_{AP_κ} is the distance form ***R*** to AP_κ, $n_\kappa \sim \mathcal{CN}(0, \sigma^2)$ is the additive white Gaussian noise (AWGN) at AP_κ.

Without the loss of generality, we assume $\eta_t > \eta_r$. The successive interference cancellation (SIC) technique is applied to decode the received signals at ***APs***. Thus, the signal x_t is decoded first, and x_r is treated as interference. After that, x_t is removed from the received signal, and the ***APs*** proceed to decode x_r. Note that ***APs*** can remove the AN signal because they are legitimate devices in the network [13]. From there, the signal-to-interference-plus-noise ratio (SINR) at AP_t and the signal-noise ratio (SNR) at AP_r are written as:

$$\gamma_{AP_t}^{x_t} = \frac{\eta_t\gamma_t\left|\mathbf{h}_{UR}^{t}\Theta^{t}\mathbf{h}_{RAP_t}\right|^2}{\eta_r\gamma_t\left|\mathbf{h}_{UR}^{t}\Theta^{t}\mathbf{h}_{RAP_t}\right|^2+1}, \quad (6)$$

$$\gamma_{AP_r}^{x_r} = \eta_r\gamma_r\left|\mathbf{h}_{UR}^{r}\Theta^{r}\mathbf{h}_{RAP_r}\right|^2, \quad (7)$$

where $\gamma_\kappa = \frac{\gamma_0}{\mathbb{L}_{UR}d_{AP_\kappa}^{\alpha}}, \gamma_0 = \frac{P_U}{\sigma^2}, \kappa \in \{t, r\}$.

We assume that ***E*** can not remove the AN, thus, the SINR at ***E*** used to decode the signal x_r is:

$$\gamma_E^{x_r} = \frac{\eta_r\gamma_E\left|\mathbf{h}_{UR}^{r}\Theta^{r}\mathbf{h}_{RE}^{r}\right|^2}{\eta_j\gamma_E\left|\mathbf{h}_{UR}^{r}\Theta^{r}\mathbf{h}_{RE}^{r}\right|^2+1}, \quad (8)$$

Where $\gamma_E = \frac{\gamma_0}{\mathbb{L}_{UR}d_E^{\alpha}}$.

The offloading time of a task from ***U*** to AP_κ is $t_{1\kappa} = \frac{L_\kappa}{C_{AP_\kappa}}$, where C_{AP_κ} is denoted by the channel capacity from ***U*** to AP_κ; L_κ is the offloaded task length to AP_κ. Let L is the total task length of ***U***, and χ is the task division ratio, thus $L_t = \chi L$, and $L_r = (1 - \chi)L$. The computational latency can be written as $\frac{\omega_\kappa L_\kappa}{f_\kappa}$, where ω_κ is denoted as the number of CPU cycles required to process one bit input, f_κ is the CPU frequency at AP_κ. Moreover, the computational result return time is too small compared to the above two time intervals, so it can be ignored [14]. Since the entire communication process must be less than a threshold T_{th}, we can write the expression as $t_{AP_\kappa} = t_{1\kappa} + \frac{\omega_\kappa L_\kappa}{f_\kappa}$.

The instantaneous security capacity is presented as $C_{AP_r,E} = \left[C_{AP_r} - C_E\right]^+$ [15], where $C_{AP_r} = W\log_2\left(1+\gamma_{AP_r}^{x_r}\right)$ and $C_E = W\log_2\left(1+\gamma_E^{x_r}\right)$, $[x]^+ = \max\{0, x\}$, W is the bandwidth.

3. Performance analysis

In this section, to evaluate the security performance of STAR-RIS-based NOMA MEC networks using the secrecy successful computation probability (SSCP) metric, denoted as Λ_S. SSCP is defined that the time all tasks are completed is less than the allowed threshold time T_{th}, and the instantaneous security capacity is higher than a security rate threshold R_{th}. Therefore, Λ_S serves as a critical indicator, simultaneously quantifying the reliability of task completion within latency constraints and the robustness of the communication link against potential eavesdropping attacks in our secure offloading framework. Mathematically, SSCP is formulated as follows [16]:

$$\Lambda_S = \Pr\left(\max\left(t_{AP_t}, t_{AP_r}\right) \le T_{th}, C_{AP_r,E} > R_{th}\right) \quad (9)$$

The closed-form expression of SSCP is described in **Theorem 1.**

Theorem 1. *The SSCP of the proposed secrecy STAR-RIS-aided NOMA MEC system is as follows:*

$$\Lambda_S = \begin{cases} I_1\left(I_{2a}+I_{2b}\right), & \Psi_r a_1 > B \\ I_1\left(I_{2c}+I_{2d}\right), & \Psi_r a_1 < B \\ 0, & otherwise \end{cases}, \quad (10)$$

where

$$I_1 = 1-F_{X_t}\left(\Psi_t\right), I_{2a} = \left[1-F_{X_r}\left(\Psi_r\right)\right]\left[1-F_{X_E}\left(\Phi\right)\right],$$

$$I_{2b} = F_{X_E}\left(\Phi\right) - \sum_{l_r=0}^{\infty}\sum_{l_E=0}^{\infty}\sum_{q=1}^{Q}\frac{\pi\Phi e^{-\frac{\lambda_r+\lambda_E-t_q}{2}}\lambda_r^{l_r}\lambda_E^{l_E}\gamma\left(l_r+\frac{1}{2},\frac{A+Bt_q}{2\left(a_1 t_q+a_2\right)}\right)t_q^{l_E-\frac{1}{2}}\sqrt{1-x_q^2}}{2Ql_r!l_E!2^{l_r+2l_E+\frac{1}{2}}\Gamma\left(l_r+\frac{1}{2}\right)\Gamma\left(l_E+\frac{1}{2}\right)}$$

$$I_{2c} = \left[1-F_{X_r}\left(\Psi_r\right)\right]F_{X_E}\left(\Phi\right),$$

$$I_{2d} = 1-F_{X_E}\left(\Phi\right) - \sum_{l_r=0}^{\infty}\sum_{l_E=0}^{\infty}\sum_{k=1}^{K}\frac{\pi e^{-\frac{\lambda_r+\lambda_E+\mathcal{G}_k}{2}}\lambda_r^{l_r}\lambda_E^{l_E}\gamma\left(l_r+\frac{1}{2},\frac{A+B\mathcal{G}_k}{2\left(a_1\mathcal{G}_k+a_2\right)}\right)\mathcal{G}_k^{l_E-\frac{1}{2}}}{Kl_r!l_E!2^{l_r+2l_E+\frac{1}{2}}\Gamma\left(l_r+\frac{1}{2}\right)\Gamma\left(l_E+\frac{1}{2}\right)}\sqrt{\frac{1-x_k}{1+x_k}},$$

$$\Psi_t = \frac{\Omega_t}{\gamma_t\left[\eta_t-\eta_r\Omega_t\right]}, \Psi_r = \frac{\Omega_r}{\eta_r\gamma_r}, \Omega_t = 2^{\frac{L_t}{WT_t}}-1, \Omega_r = 2^{\frac{L_r}{WT_r}}-1,$$

$$T_t = T_{th}-\frac{\omega_t L_t}{f_t}, T_r = T_{th}-\frac{\omega_r L_r}{f_r}, A = 2^{\frac{R_S}{W}}-1, B = \left[2^{\frac{R_{Se}}{W}}\left(\eta_r+\eta_j\right)-\eta_j\right]\gamma_E,$$

$$a_1 = \eta_r\eta_j\gamma_r\gamma_E, a_2 = \eta_r\gamma_r, \Phi = \frac{A-\Psi_r a_2}{\Psi_r a_1 - B}, x_q = \cos\left(\frac{2q-1}{2Q}\pi\right),$$

$$t_q = \frac{x_q+1}{2}\Phi, x_k = \cos\left(\frac{2k-1}{K}\pi\right), t_k = \frac{x_k+1}{2}, \mathcal{G}_k = \Phi - \ln\left(t_k\right),$$

Q and K are the complexity-vs-accuracy trade-off coefficient.

Proof. See Appendix A.

4. Numerical results and discussion

This section employs the Monte Carlo simulations to assess the secrecy performance of the NOMA-based UAV-enabled MEC STAR-RIS network. We establish the simulation parameters focus on the realistic data [17, 18, 19], which are specifically described in Table 1.

Figure 2 demonstrates the influence of the average transmit SNR (γ_0) on the SSCP under three different numbers of RIS element (N). As the average transmit SNR increases, so does the transmit power, which significantly enhances system performance. This improvement stems from the increased SNR at the ***APs***, elevating their capacity to compute tasks, as indicated by the expressions (6) and (7). However, it is important to note that when the average transmit SNR reaches a certain threshold for each N value, the performance tends to saturate, highlighting the need to consider energy conservation in communication. Furthermore, a clear trend emerges across the three different N values: a larger N corresponds to more outstanding performance.

Table 1. *Typical values of simulation parameters*

Parameter	Value	Parameter	Value
(x_U, y_U, h_U)	(0, 0, 0 - 50)	L	0.1 Mb
(x_R, y_R, h_R)	(10, 30, 15)	χ	0.4, 0.6, 0.8
$(x_{AP_t}, y_{AP_t}, h_{AP_t})$	(20, 50, 5)	σ^2	-50 dBm
$(x_{AP_r}, y_{AP_r}, h_{AP_r})$	(30, 15, 5)	P_U	0 - 15 dB
(x_E, y_E, h_E)	(55, 20, 0)	N	20 - 40
ξ_{LoS}, ξ_{NLoS}	1, 20	T_{th}	70 - 150 ms
ζ, ϑ	9.61, 0.15	R_{th}	0.1 Mbps
f_c	2 GHz	$m_{UR}^{\kappa}, m_{RAP_t}, m_{RAP_r}, m_{RE}$	1-3
c	3×10^8 m/s	α	2
η_t, η_r, η_j	0.5, 0.3, 0.2	β^t, β^r	0.5, 0.5
f_t, f_r	1 GHz	W	1 MHz
ω_t, ω_r	2	Q, K	100

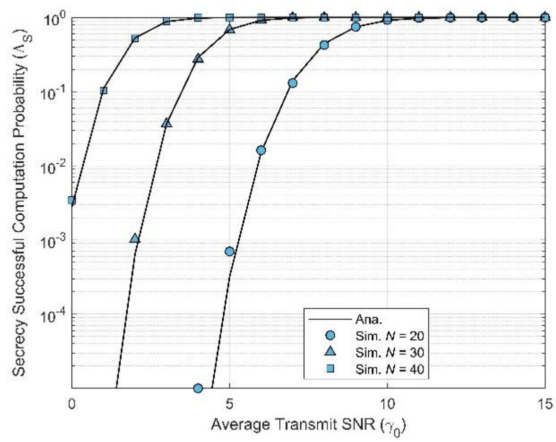

Figure 2. *SSCP versus the average transmit SNR with different numbers of RIS elements*

Figure 3 illustrates the influence of the height of ***U*** (h_U) on system performance with different task division ratios (χ). When h_U increases, SSCP increases in all three investigated cases, but after the optimal altitude of ***U***, it tends to decrease. This is explained by the fact that when h_U is low, the probability of LoS is low, the probability of NLoS is high, causing the connection between nodes to be limited, and when h_U increases, the opposite is true, but when reaching the height of, SSCP decreases because the path loss is too large, leading to weaker communication links. In Figure 3, three levels of χ are also examined, namely 0.4, 0.6, and 0.8. An interesting result appears when $\chi = 0.6$, where the SSCP achieves its best value. This suggests the existence of an optimal task division ratio, and ***U*** needs to incorporate analytical techniques to find that coefficient, to ensure balance and optimality when performing offloading.

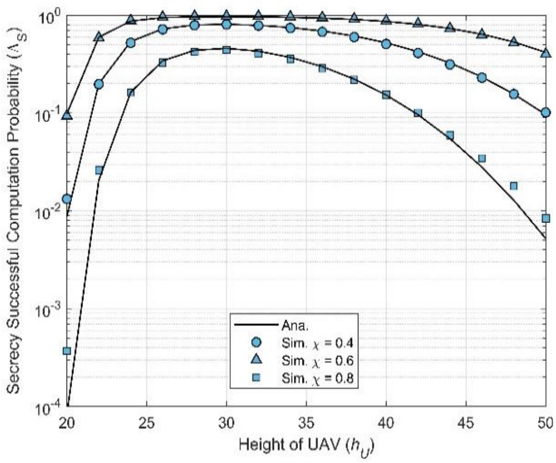

Figure 3. *SSCP versus the height of U with various task division ratios*

Figure 4 illustrates the effect of the AN on SSCP. We fixed the value of $\eta_t = 0.5$ to investigate and examine the system performance according to the parameter η_j. Note that when $\eta_j = 0$ corresponds to the case where ***U*** does not transmit AN. The investigation results show that as n_j increases, SSCP increases, reaches the maximum value, and tends to decrease as η_j continues to increase. It is explained by the fact that when η_j is low, the noise at *E* is 0, leading to a high probability of *E* decoding information at AP_r. When η_j increases, the noise at *E* increases, thereby improving SSCP. However, when η_j increases too much, it decreases energy allocation to AP_r, weakening the ability to calculate tasks at AP_r and reducing SSCP. Hence, we must consider allocating energy to reduce task load and energy to AN to maximise performance. In addition, Figure 4 examines three different lengths of task (*L*) levels when *L* has lengths of 0.08 Mb, 0.09 Mb, and 0.1 Mb, respectively. It is clear that the larger the task size, the lower the SSCP will be because the more significant *L* is, the more time we need to calculate the task.

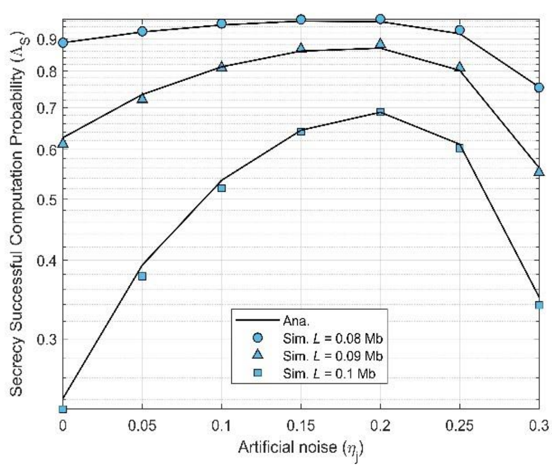

Figure 4. *SSCP versus the AN with various lengths of tasks*

Figure 5 illustrates the effect of the threshold time (T_{th}) over various Nakagami-*m* fading shape factor conditions. For simplicity, we set $m_{UR}^{\kappa} = m_{RAP_t} = m_{RAP_r} = m_{RE} \triangleq m$ in this investigation. The simulation results demonstrate that a higher value of *m* leads to improved system performance. It is important to note that the Nakagami-*m* channel is a generalized fading channel; therefore, from the analytical results derived in Theorem 1, the system performance over Rayleigh fading can be readily inferred by setting *m* = 1. It should be further emphasized that the Rayleigh channel describes the most severe fading scenario, representing the poorest transmission channel with a high probability of deep fades. As *m* increases, the Nakagami-*m* distribution transitions from a Rayleigh distribution towards a Gaussian distribution, implying a reduction in signal strength fluctuations and a significant decrease in the probability of deep fading, consequently enhancing system performance.

Furthermore, Figure 5 depicts the impact of T_{th} on system performance: a higher T_{th} results in a higher SSCP, and vice versa. Evidently, a low T_{th} represents applications with very stringent response time constraints. In contrast, when this parameter is sufficiently large, the system has more time for offloading and computation, leading to an overall improvement in performance.

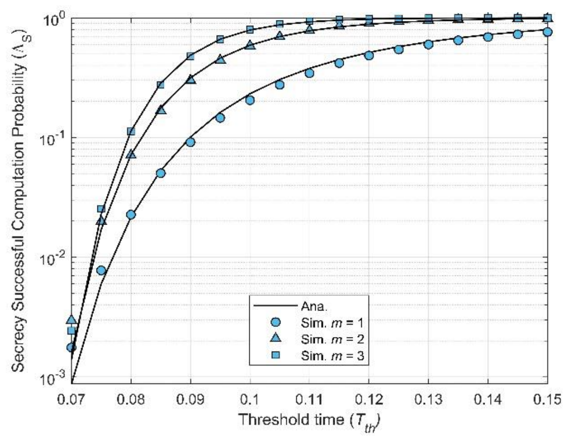

Figure 5. *SSCP versus the threshold time with various Nakagami fading shape factor*

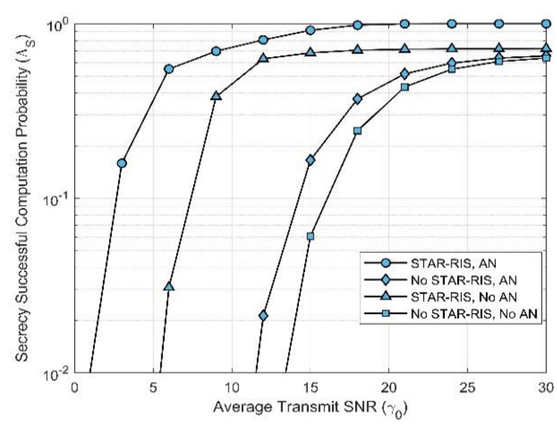

Figure 6. *Comparison of SSCP of the proposed model with different baseline network models*

Figure 6 compares the performance of the STAR-RIS-aided AN-based UAV NOMA MEC architecture with various baseline schemes. Specifically, this investigation compares four distinct scenarios: (i) the proposed scheme of this paper, i.e., UAV NOMA MEC employing STAR-RIS and AN, (ii) the UAV NOMA MEC scheme employing only AN, (iii) the UAV NOMA MEC scheme employing only STAR-RIS, and (iv) a baseline UAV NOMA MEC scheme. The simulation results reveal that the system performance of the proposed architecture, with the incorporation of STAR-RIS and the utilization of AN, significantly outperforms the other cases. Further analysis indicates that the two scenarios without STAR-RIS (cases (ii) and (iv)) exhibit lower performance compared to their respective counterparts that utilize STAR-RIS (cases (i) and (iii)). Similarly, the two scenarios without AN (cases (iii) and (iv)) demonstrate inferior performance compared to their respective counterparts that incorporate AN (cases (i) and (ii)). These findings corroborate the effectiveness of our proposed model.

The simulation results from Figure 2 to Figure 6 are in perfect agreement with the computational theory we presented. Furthermore, the Monte Carlo parameter set changes do not significantly affect the overall observable trend of the proposed system.

5. Conclusion

In this paper, we investigated a secrecy NOMA-based STAR-RIS UAV-enabled MEC network. The system employed a STAR-RIS with ES protocol for simultaneous transmission and reflection and AN transmission from the UAV to enhance security. We derive the approximate closed-form expressions for the SSCP and use this metric to evaluate secrecy system performance. We investigated the impact of critical parameters such as transmit power, number of RIS elements, task division ratio, UAV altitude, and task length. The investigation is further validated via Monte-Carlo simulations. The findings of this study highlight that by optimizing UAV altitude and power allocation, the system demonstrated significant improvement in secrecy performance. It emphasises the potential of integrating STAR-RIS technology with UAV-enabled MEC networks to achieve secure and efficient communication in the presence of eavesdroppers.

Acknowledgement: The authors would like to express their sincere gratitude to Duy Tan University for their invaluable support in conducting this research.

REFERENCES

[1] S. M. Mohammed, A. Al-Barrak, and N. T. Mahmood, “Enabling technologies for ultra-low latency and high-reliability communication in 6g networks”, *Ingenierie des Systemes d’Information*, vol. 29, no. 3, 2024.

[2] M. H. Adnan, Z. A. Zukarnain, and O. A. Amodu, “Fundamental design aspects of uav-enabled mec systems: A review on models, challenges, and future opportunities”, *Computer Science Review*, vol. 51, p. 100615, 2024.

[3] T. Van Truong, A. Nayyar, M. Bilal, and K. S. Kwak, “System design and optimization of mobile edge computing in the noma wireless tactile internet of things network”, *Alexandria Engineering Journal*, vol. 73, pp. 737–749, 2023.

[4] H. Xiao, X. Hu, W. Wang, Z. Su, K.-K. Wong, and K. Yang, “STAR-RIS and UAV combination in MEC networks: Simultaneous task offloading and communications”, *IEEE Transactions on Communications*, 2025. https://doi.org/10.1109/TCOMM.2025.3535895.

[5] X. Deng *et al*, “Energy-efficient strategic UAV-enabled mec networks via starris: Joint optimization of trajectory and user association”, *IEEE Internet of Things Journal*, vol. 12, no. 10, pp. 14921-14937, 2025.

[6] F. R. Ghadi, F. J. Lopez-Martınez, and K.-K. Wong, “Analytical characterization of coverage regions for star-ris-aided noma/oma communication systems”, *IEEE Communications Letters*, vol. 27, no. 11, pp. 3063-3067, 2023.

[7] H. Lei, M. Yang, J. Jiang, K.-H. Park, and G. Pan, “Secure offloading in noma-aided aerial mec systems based on deep reinforcement learning”, *IEEE Journal on Miniaturization for Air and Space Systems*, vol. 6, no. 2, pp. 113-124, 2025.

[8] M. Diamanti, E. E. Tsiropoulou, and S. Papavassiliou, "Resource orchestration in UAV-assisted NOMA wireless networks: A labor economics perspective", *ICC 2021-IEEE International Conference on Communications*, pp. 1-6, 2021.

[9] Q.-H. Nguyen-Anh, A.-N. Nguyen, and D.-B. Ha, “Joint secrecy and latency performance analysis for uav-assisted uplink noma-based iot network with mobile edge computing”, in *International Conference on Industrial Networks and Intelligent Systems*. Springer, 2024, pp. 236–255.

[10] D. Krstic, Z. Jovanovic, R. Gerov, M. Stefanovic, and M. Gligorijevic, “Performance analysis of wireless communication system in the presence of gamma shadowing, nakagami-m multipath fading and cochannel interference”, *International Journal of Communications*, vol. 1, pp. 150–157, 2016.

[11] G. Zhu, X. Mu, L. Guo, A. Huang, and S. Xu, “Enhancing user fairness in wireless powered communication networks with star-ris”, *IEEE Internet of Things Journal*, vol. 12, no. 3, pp. 2659-2673, 2024.

[12] S.-P. Le, H.-N. Nguyen, N.-T. Nguyen, C. H. Van, A.-T. Le, and M. Voznak, “Physical layer security analysis of irs-based downlink and uplink noma networks”, *EURASIP Journal on Wireless Communications and Networking*, vol. 2023, no. 1, p. 105, 2023.

[13] Y. Liu, Z. Qin, M. Elkashlan, Y. Gao, and L. Hanzo, “Enhancing the physical layer security of non-orthogonal multiple access in large-scale networks”, *IEEE Transactions on Wireless Communications*, vol. 16, no. 3, pp. 1656–1672, 2017.

[14] V.-T. Truong and T.-N. Nguyen, “Secrecy performance analysis of rf energy harvesting uav-enabled noma mec system under eavesdropping scenario”, in *2024 IEEE International Conference on Consumer Electronics-Asia (ICCE-Asia)*. IEEE, 2024, pp. 1–4.

[15] K. Jiang, T. Jing, Y. Huo, F. Zhang, and Z. Li, “SIC-based secrecy performance in uplink NOMA multi-eavesdropper wiretap channels”, *IEEE Access*, vol. 6, pp. 19664-19680, 2018.

[16] V.-T. Truong, D.-B. Ha, and M.-T. Vo, “Rf energy harvesting and security offloading protocol for mec-enabled noma networks with passive eavesdropper”, in *2023 International Conference on Advanced Technologies for Communications (ATC)*. IEEE, 2023, pp. 51–56.

[17] H. Xiao, X. Hu, W. Zhang, W. Wang, K.-K. Wong, and K. Yang, “Energy-efficient STAR-RIS enhanced UAV-enabled MEC networks with bi-directional task offloading”, *IEEE Transactions on Wireless Communications*, vol. 24, no. 4, pp. 3258-3272, 2025

[18] M. Sohail, C. Leow, & S. Won, “Non-orthogonal multiple access for unmanned aerial vehicle assisted communication”, *IEEE Access*, vol. 6, pp. 22716-22727, 2018.

[19] Z. Bouida, I. AlShiab, Y. Rafique, A. Jarwan, M. Moorjmalani, S. Kuri, & M. Ibnkahla, “Carleton-Cisco IoT testbed: Architecture, features, and applications”, In Proc. *2021 IEEE Globecom Workshops (GC Wkshps*, IEEE, 2021*)*, 2021, pp. 1-6.

APPENDIX A: PROOF OF THEOREM 1

In this section, we present the proof of **Theorem 1**. From the SSCP definition formula (9), we have:

$$\begin{aligned}\Lambda_S &= \Pr\left(\frac{L_t}{C_{AP_t}} \le \underbrace{T_{th} - \frac{\omega_t L_t}{f_t}}_{T_t}, \frac{L_r}{C_{AP_r}} \le \underbrace{T_{th} - \frac{\omega_r L_r}{f_r}}_{T_r}, C_{AP_r} - C_E > R_{th}\right) \\ &= \Pr\left(\frac{\eta_t\gamma_t X_t}{\eta_r\gamma_t X_t + 1} \ge \underbrace{2^{\frac{L_t}{WT_t}} - 1}_{\Omega_t}, \eta_r\gamma_r X_r \ge \underbrace{2^{\frac{L_r}{WT_r}} - 1}_{\Omega_r}, \frac{1+\eta_r\gamma_r X_r}{1+\frac{\eta_r\gamma_E X_E}{\eta_j\gamma_E X_E + 1}} > 2^{\frac{R_{th}}{W}}\right) \\ &= \begin{cases} \Pr\left(X_t \ge \underbrace{\frac{\Omega_t}{\gamma_t\left[\eta_t - \eta_r\Omega_t\right]}}_{\Psi_t}, X_r \ge \underbrace{\frac{\Omega_r}{\eta_r\gamma_r}}_{\Psi_r}, \frac{1+\eta_r\gamma_r X_r}{\frac{\eta_j\gamma_E X_E + 1 + \eta_r\gamma_E X_E}{\eta_j\gamma_E X_E + 1}} > 2^{\frac{R_{th}}{W}}\right), & \frac{\eta_t}{\eta_r} > \Omega_t \\ 0, & \frac{\eta_t}{\eta_r} \le \Omega_t \end{cases}\end{aligned} \tag{A-1}$$

where $\gamma_\kappa = \frac{\gamma_0}{\mathbb{L}_{UR} d_{AP_\kappa}^{\alpha}}, \gamma_E = \frac{\gamma_0}{\mathbb{L}_{UR} d_E^{\alpha}}, \kappa \in \{t, r\}$.

We focus the case $\frac{\eta_t}{\eta_r} > \Omega_t$, hence SSCP is rewritten as follows:

$$\begin{aligned}\Lambda_S &= \Pr\left(\begin{array}{l} X_t \ge \Psi_t, X_r \ge \Psi_r, \\ X_r\left(\underbrace{\eta_r\eta_j\gamma_r\gamma_E}_{a_1} X_E + \underbrace{\eta_r\gamma_r}_{a_2}\right) > \underbrace{2^{\frac{R_{th}}{W}} - 1}_{A} + \underbrace{\left[2^{\frac{R_{th}}{W}}\left(\eta_r + \eta_j\right) - \eta_j\right]\gamma_E}_{B} X_E \end{array}\right) \\ &= \Pr\left(X_t \ge \Psi_t, X_r \ge \Psi_r, X_r > \frac{A + BX_E}{a_1 X_E + a_2}\right) \\ &= \underbrace{\left[1 - F_{X_t}(\Psi_t)\right]}_{I_1} \underbrace{\Pr\left(X_r \ge \Psi_r, X_r > \frac{A + BX_E}{a_1 X_E + a_2}\right)}_{I_2}\end{aligned} \tag{A-2}$$

We observe that I_1 is easily obtained using (3). We calculate the integral I_2 as follows:

$$\begin{aligned} I_2 &= \Pr\left(X_r \ge \Psi_r, X_r > \frac{A + BX_E}{a_1 X_E + a_2}\right) \\ &= \begin{cases} \Pr\left(X_r \ge \Psi_r, X_E > \Phi\right) + \Pr\left(X_r > \frac{A + BX_E}{a_1 X_E + a_2}, X_E < \Phi\right) & \Psi_r a_1 > B \\ \Pr\left(X_r \ge \Psi_r, X_E < \Phi\right) + \Pr\left(X_r > \frac{A + BX_E}{a_1 X_E + a_2}, X_E > \Phi\right) & \Psi_r a_1 < B \end{cases} \\ &= \begin{cases} \underbrace{\left[1 - F_{X_r}(\Psi_r)\right]\left[1 - F_{X_E}(\Phi)\right]}_{I_{2a}} + \underbrace{\int_0^{\Phi}\left[1 - F_{X_r}\left(\frac{A + Bx}{a_1 x + a_2}\right)\right] f_{X_E}(x)\,dx}_{I_{2b}} & \Psi_r a_1 > B \\ \underbrace{\left[1 - F_{X_r}(\Psi_r)\right] F_{X_E}(\Phi)}_{I_{2c}} + \underbrace{\int_{\Phi}^{\infty}\left[1 - F_{X_r}\left(\frac{A + Bx}{a_1 x + a_2}\right)\right] f_{X_E}(x)\,dx}_{I_{2d}} & \Psi_r a_1 < B \end{cases}\end{aligned} \tag{A-3}$$

The expressions I_{2a} and I_{2c} are effortlessly obtained using (3). We continue to present the computation of the expression I_{2b} as follows, noting that in step (*), we applied the Gaussian-Chebyshev quadrature method:

$$\begin{aligned} I_{2b} &= \int_0^{\Phi} f_{X_E}(x)\,dx - \int_0^{\Phi} F_{X_r}\left(\frac{A + Bx}{a_1 x + a_2}\right) f_{X_E}(x)\,dx \\ &= F_{X_E}(\Phi) - \int_0^{\Phi} e^{-\frac{\lambda_r}{2}} \sum_{l_r=0}^{\infty} \frac{\lambda_r^{l_r}\gamma\left(l_r + \frac{1}{2}, \frac{A + Bx}{2(a_1 x + a_2)}\right)}{l_r! 2^{l_r}\Gamma\left(l_r + \frac{1}{2}\right)} e^{-\frac{x + \lambda_E}{2}} \sum_{l_E=0}^{\infty} \frac{\lambda_E^{l_E} x^{l_E - \frac{1}{2}}}{l_E! 2^{2l_E + \frac{1}{2}}\Gamma\left(l_E + \frac{1}{2}\right)}\,dx \\ &\overset{(*)}{=} F_{X_E}(\Phi) - \sum_{l_r=0}^{\infty}\sum_{l_E=0}^{\infty}\sum_{q=1}^{Q} \frac{\pi\Phi}{2Q} \frac{e^{-\frac{\lambda_r + \lambda_E + t_q}{2}} \lambda_r^{l_r}\lambda_E^{l_E}\gamma\left(l_r + \frac{1}{2}, \frac{A + Bt_q}{2\left(a_1 t_q + a_2\right)}\right)}{l_r! l_E! 2^{l_r + 2l_E + \frac{1}{2}}\Gamma\left(l_r + \frac{1}{2}\right)\Gamma\left(l_E + \frac{1}{2}\right)} t_q^{l_E - \frac{1}{2}} \sqrt{1 - x_q^2}\end{aligned} \tag{A-4}$$

The expression I_{2d} is proven the same as above. This proof is over.